Journal of Energy Storage 130 (2025) 117226

Contents lists available at ScienceDirect

Journal of Energy Storage

journal homepage: www.elsevier.com/locate/est

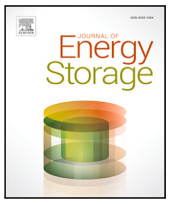

Research papers

Geotechnical gravity energy storage (GGES): A proof of concept using holistic numerical simulations

L. Mugele *, H.H. Stutz

Institute of Soil Mechanics and Rock Mechanics (IBF), Karlsruhe Institute of Technology (KIT), Engler-Bunte-Ring 14, Karlsruhe, 76131, Baden-Württemberg, Germany

ARTICLE INFO

Keywords:
Geotechnical gravity energy storage (GGES)
Energy transition
Cyclic deformations
Hypoplasticity
High-cycle accumulation model

ABSTRACT

The global energy transition requires significant energy storage capacity to mitigate the natural fluctuations of renewable energy such as photovoltaic and wind power caused by alternating weather patterns. This paper presents the innovative concept of the so-called geotechnical gravity energy storage (GGES) system. In this concept, excess renewable electrical energy is stored as potential energy of an elevated mass of soil in the underground space using a pressurized fluid pumped in a soil-covered cavity. Due to the high pressure in the fluid, induced by an overburden height of several hundreds of meters, the resulting displacements and deformations at the ground surface can be kept small. A turbine regenerates the stored electrical energy on demand. Numerical simulations using a hypoplastic and a high-cycle accumulation constitutive model for sand are presented and demonstrate the system's ability to store several MWh of energy combined with negligible energy losses within the soil, even after 40 000 simulated energy storage cycles. As a reference variant, a GGES system with a capacity of up to ≈ 5 MWh and a soil mechanical efficiency of $\eta \approx 98\%$ is investigated. The overall efficiency - including additional energy losses due to pipe friction and energy transition - of a GGES system is comparable to that of a conventional pumped hydro energy storage (PHES) system. The GGES concept is scalable, and much larger energy storage capacities can be achieved in reality. Notably, the efficiency of the GGES system increases with increasing lifetime and soil compaction effects occur. The GGES system shows positive degradation effects, which distinguishes it from most existing energy storage systems. The results provide a simple design formula for a GGES and depict the geometric and operation limits within which the long-term stability of the system is guaranteed. For systems with a height-to-radius ratio of $H/R > 2$, operated at a soil mechanical efficiency of $\eta > 95\%$, the stability of the GGES system is demonstrated and failure can be excluded.

1. Introduction

The ongoing global energy transition includes sustained growth in the installed capacity of renewable energy sources (RES), particularly photovoltaic and wind energy [1]. The share of RES in public electricity generation in the European Union increased over the past five years from 30.5% in 2018 to about 42.3% in 2023 [2,3], while globally, the share of RES in the electricity sector was 29% in 2020 [1]. RES contribute to sustainability by reducing greenhouse gas emissions, minimizing environmental impacts, and addressing economic as well as social needs [4,5]. To mitigate climate change, it is essential to sustain and accelerate this trend [1]. For instance, as part of the European Green Deal, the European Union aims to achieve net-zero greenhouse gas emissions by 2050.

However, the energy supply from RES is subject to significant natural fluctuations caused by changing weather conditions [6]. To maintain the reliability of energy supply and grid stability, even with an increasing share of renewable energy in the future, the demand for energy storage capacity will continue to grow. Energy storage systems allow excess renewable energy to be stored during periods of high energy production and utilized later at times when energy demand exceeds production. Today, various technologies exist for storing excess electrical energy, including chemical, electrochemical, electrical, thermal, and mechanical methods [7,8]. The latter includes the well-known pumped hydro energy storage (PHES) system, which is currently the most widely used large-scale solution for excess electrical energy storage [9,10]. As shown in Fig. 1a, the basic concept of PHES is to use surplus energy to pump water to a higher elevation, thereby storing potential energy. The electrical energy can later be regenerated using a turbine. Modern PHES systems achieve an efficiency of about

* Corresponding author.
E-mail addresses: luis.mugele@kit.edu (L. Mugele), hans.stutz@kit.edu (H.H. Stutz).

https://doi.org/10.1016/j.est.2025.117226
Received 17 December 2024; Received in revised form 29 April 2025; Accepted 25 May 2025
Available online 18 June 2025
2352-152X/© 2025 The Authors. Published by Elsevier Ltd. This is an open access article under the CC BY-NC license (http://creativecommons.org/licenses/by-nc/4.0/).

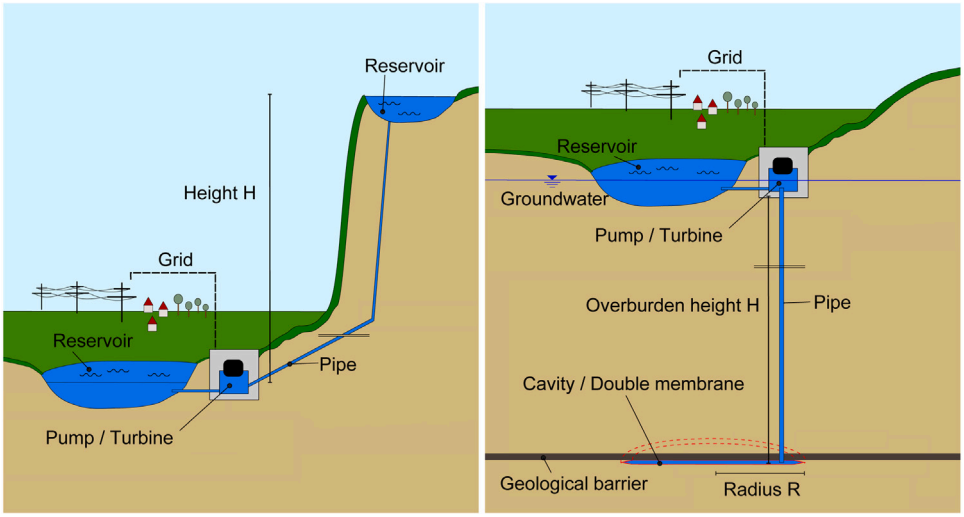

Fig. 1. Illustration of (a) the conventional pumped hydro energy storage (PHES) system and (b) the novel geotechnical gravity energy storage (GGES) system.

80% [7,9]. However, PHES technology has limitations, as it requires a specific topography and occupies a considerable amount of land. As a result, there is a growing need to investigate and develop alternative energy storage technologies.

This work presents the innovative geotechnical gravity energy storage (GGES) system, a large-scale energy storage technology also referred to as an earth battery [11]. The concept is based on the idea of the underground pumped hydro energy storage (UPHES) system, where energy is stored by lifting a soil mass through the pumping of water into a cavity covered by soil. UPHES systems have already been investigated using model experiments [12,13], centrifuge tests [14], and numerical simulations [15,16]. It has already been shown that UPHES systems achieve a similar efficiency to conventional PHES systems [12–14]. The installation costs were estimated in 2015 to 1111 €/kW for power capacity and 208 €/kWh for storage capacity [12]. In 2022, the investment costs were estimated to range between 125 and 190 €/kWh [17]. Thereby the primary cost driver identified is soil movement. Although these values should be interpreted with caution, they highlight the economic potential of the technology.

Compared to these, the GGES system aims to further increase the energy storage capacity and efficiency by increasing the overburden height and reducing the deformation of the overburden soil. The GGES concept is illustrated in Fig. 1b. The key element of the GGES system is a so-called double membrane, which forms a cavity in the underground. This crucial element of the GGES system is located at depths of several hundred meters below the ground surface directly beneath a geological barrier characterized by low permeability (e.g. an over-consolidated layer of clay or claystone) and serves as a load distribution layer. Two technical installation concepts for the double membrane are currently under research:

- Synthetic membrane (geomembrane) placed in an existing excavation before backfilling: The concept of using a geomembrane was previously tested in the UPHES system [12–14,17], as shown in Fig. 2a. However, the possible membrane failure observed in the UPHES system is attributed to large strains within the membrane [12,17], is unlikely to occur in the GGES system due to significantly reduced deformation. Open-cast mines or quarries may provide suitable sites for the installation of the synthetic membrane.
- Clay-like membrane installed from the surface by injecting a clay (bentonite) suspension into a borehole [11]: This novel technique, which was recently patented [18] and experimentally investigated [19], allows the construction of the double membrane and cavity at almost any depth and site characteristics. The formation of the clay-like membrane is based on the consolidation processes of a bentonite suspension. Recently, the clay-like membrane was successfully produced on a laboratory scale by injecting the bentonite suspension into a sand layer under high pressures (several bars), as shown in Fig. 2b. Within a few minutes of injection, a thin, highly consolidated clay layer (clay-like membrane) forms, exhibiting ductile behavior and very high impermeability. While this method is promising, further comprehensive studies are still pending. One major advantage of the clay-like membrane over the geomembrane is that it can be easily repaired during the operation of a GGES system by re-injecting a suspension into the cavity or by using a fluid containing a small amount of clay (bentonite) particles.

The radius of the cavity can reach several hundred meters and the cavity can be filled (charged) and emptied (discharged) using a pressurized fluid (e.g., water). The pumped-in fluid volume leads to an elevation of the overburden soil, which increases the potential energy of the mass involved. The stored energy can be recovered later by discharging the fluid through a turbine. The pump/turbine system is located at the ground surface and connected to the underground cavity by a pipe. Note that the costs of a GGES system are estimated to be significantly lower than those of a UPHES system, as no additional soil movements are required [12,17]. It can therefore be assumed that the installation costs of a GGES system are below 100 EUR/kWh and more cost-effective than electrochemical energy storage systems [11,17], although a detailed cost analyses cannot be made at this stage of GGES concept. The current major cost uncertainty lies in the deep borehole required if a clay-like membrane is used. On the ground surface, only a powerhouse and a reservoir, lake, or river to maintain the water supply are needed. General cost estimates for energy storage systems can be found in the literature [1,20,21].

The energy input E_{in} during the charging progress can be calculated using the volume V of the cavity and the pressure P of the fluid in the cavity:

$$E_{\text{in}} = \int_{V_0}^{V_1} P \, \mathrm{d}V \, . \tag{1}$$

The energy loss ΔE during an individual energy storage cycle can be calculated by considering the recovered energy E_{out}:

$$\Delta E = \underbrace{\int_{V_0}^{V_1} P \, \mathrm{d}V}_{E_{\text{in}}} - \underbrace{\int_{V_1}^{V_0} P \, \mathrm{d}V}_{E_{\text{out}}} \, . \tag{2}$$

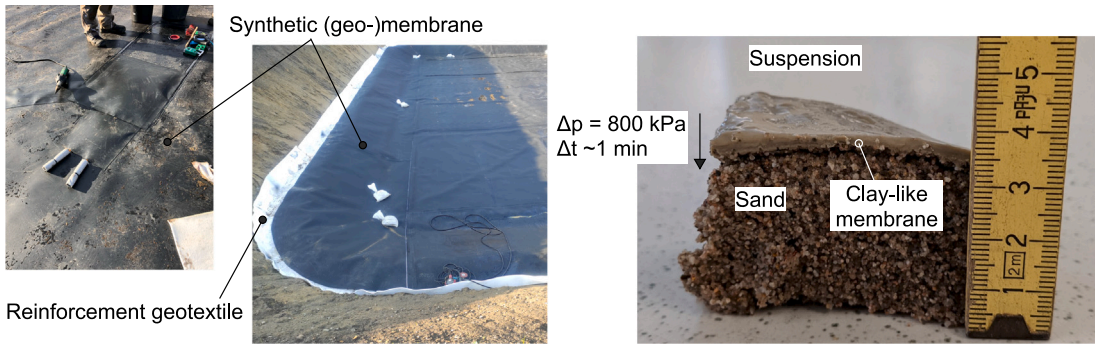

Fig. 2. Two concepts for the double membrane: (a) synthetic membrane (geomembrane) such as that tested for the UPHES system [12–14] (figures from [17]) and (b) a clay-like membrane, produced on laboratory scale under high-pressure (bentonite) suspension injection.

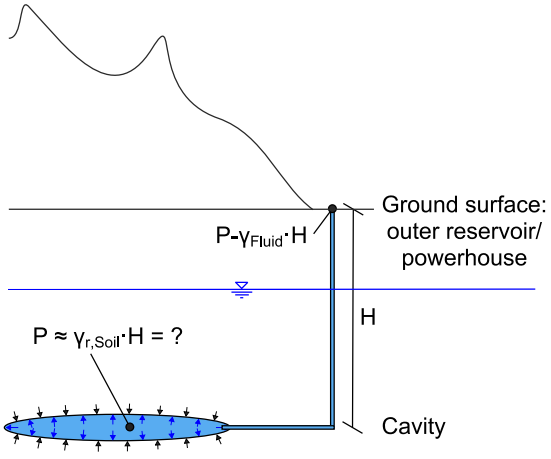

Fig. 3. Pressure distribution (without flow) in a GGES system.

The efficiency η measuring the energy loss within the soil of a GGES system can be determined:

$$\eta = \frac{E_{\text{out}}}{E_{\text{in}}} \ . \tag{3}$$

It is important to note that the elevation of the outer reservoir/the powerhouse as well as a non-horizontal ground surface will affect the usable capacity and efficiency of the overall system, as demonstrated in Fig. 3.

In contrast to other gravity energy storage (GES) systems, which typically use fluids (PHES) or rigid bodies to store energy, the GGES uses soil as the storage material. The main advantages of the GGES system over conventional GES systems include:

- minimized land use at the ground surface
- no topographical restrictions
- a protected energy infrastructure, as many components are located underground

During each energy storage cycle, the soil is not only displaced but also deformed and sheared. However, due to cyclic mechanical loading, the soil generally exhibits a rather complex mechanical behavior that is highly pressure and density-dependent. For example, both stiffness and strength increase with increasing pressure and density. In addition, accumulative effects such as cyclic densification occur due to cyclic deformations in soil, even at very small strains. Therefore, to confirm the feasibility of the GGES concept, the influence of the mechanical behavior of the overburden on the energy storage system needs to be analyzed, as such studies are not yet available in the literature.

In this paper, the feasibility of the GGES concept from a soil mechanics perspective is demonstrated through advanced numerical simulations using the finite element method (FEM). Two sophisticated constitutive models, namely the explicit high-cycle accumulation model (HCA) [22] and the implicit[1] hypoplasticity with intergranular strain model (HP+IS) [23,24], are used to simulate the complex mechanical behavior of the overburden soil. Thus, both individual energy storage cycles and cumulative effects due to high-cycle energy storage sequences have been analyzed. To evaluate the long-term behavior of the GGES system, 40 000 energy storage cycles were simulated and relevant parameters have been varied. Based on these numerical simulations, a simplified design formula for GGES systems is proposed and validated. The results indicate that energy storage capacities of several MWh can be achieved, with minimal energy losses in the overburden soil. Furthermore, only small cumulative effects are simulated.

The constitutive models used for the numerical analyses are presented in Section 2, supported by relevant element test simulations shown in Section 3. Section 4 discusses the boundary value problem of the GGES system, including the initial and boundary conditions of the simulations. The simulation results, focusing on energy capacity, efficiency, and long-term behavior under various conditions, are presented in Section 5. The results are carefully discussed in Section 6. Finally, Section 7 summarizes the key findings and provides an outlook for future research.

2. The constitutive model for soil

Soil undergoes cumulative and irreversible effects when subjected to cyclic loading with a large number of cycles (so-called high-cycle problems, $N > 300$). Depending on the problem, this can result in accumulative densification and/or stress relaxation. The cumulative behavior of soil is thereby highly nonlinear. To model such high-cycle problems, the high-cycle accumulation (HCA) model [22] was developed. The HCA calculation procedure, which consists of (A) implicit and (B) explicit phases, is described in detail in [22,25] and visualized in Fig. 4.

In conventional (A) implicit constitutive models, cyclic loading is handled incrementally in terms of stress and strain rates. As a result, they can only be used for a relatively small number of cycles (so-called low-cycle problems, $N < 50$). They are mostly not calibrated on high-cycle experiments and numerical errors can become excessive in conventional implicit simulations with a large number of cycles. These models are therefore not suitable for an accurate simulation of the cumulative effects caused by high-cyclic loading [27]. However,

[1] The terms 'explicit' and 'implicit' do not refer to a numerical integration scheme here.

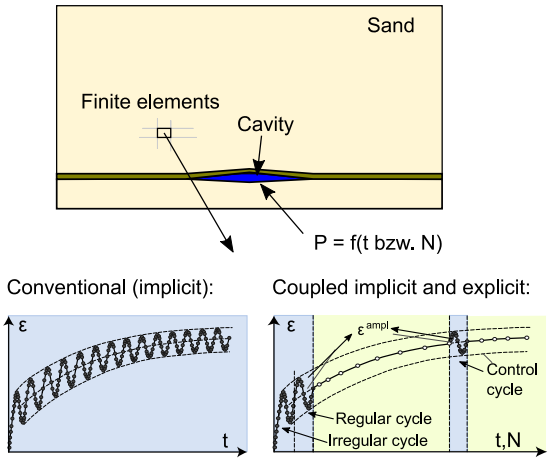

Fig. 4. The coupled (A) implicit and (B) explicit HCA calculation procedure applied to the GGES system, modified from [26].

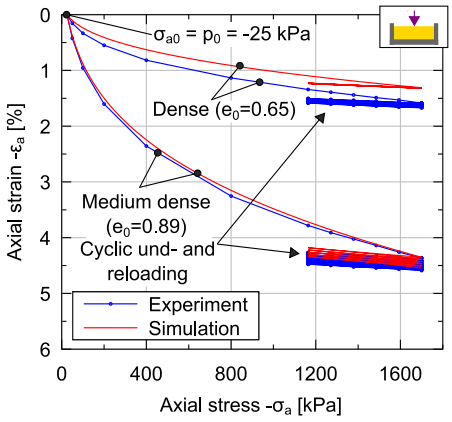

Fig. 5. Oedometric compression tests on Karlsruhe fine sand (KFS) for both loose and dense samples, with un- and reloading cycles: experimental results (blue) versus simulations using HP+IS (red).

advanced implicit constitutive models can be used effectively for the estimation of the strain amplitude caused by an individual cycle, which is one of the most important factors governing the cumulative behavior of soil. The scalar strain amplitude ϵ^{ampl} can be calculated from the strain path $\boldsymbol{\epsilon}(t)$ recorded during an implicitly calculated cycle [22], as demonstrated in Fig. 4. In this study, the hypoplastic model proposed by von Wolffersdorff [24], combined with the intergranular strain extension developed by Niemunis and Herle [23] (HP+IS), is used as the implicit constitutive model. This model uses a tensorial equation (Eq. (4)) to relate the rate of the effective Cauchy stress $\dot{\boldsymbol{\sigma}}$ to the strain rate $\dot{\boldsymbol{\epsilon}}$:

$$\dot{\boldsymbol{\sigma}} = \mathsf{M}(\boldsymbol{\sigma}, \boldsymbol{h}, e, \dot{\boldsymbol{\epsilon}}) : \dot{\boldsymbol{\epsilon}} \ . \tag{4}$$

The effective Cauchy stress $\boldsymbol{\sigma}$, the void ratio e and the intergranular strain $\boldsymbol{h}$ are utilized as state variables. A detailed explanation of the model and parameter determination is available in [23,24,28,29].

In the GGES system analyzed in this study, the scalar strain amplitude ϵ^{ampl} along with the cavity volume V and the fluid pressure P within the cavity can be determined during the implicit calculation phase. Based on this, the energy capacity and efficiency of the entire GGES system can be estimated as outlined in Eqs. (1)–(3). The first (irregular) cycle typically leads to larger deformations than the following (regular) cycles. Therefore, at least two cycles must be simulated using the implicit model at the beginning of an HCA simulation. The strain path needed to determine the strain amplitude is recorded during the second cycle, which serves as the first regular cycle. So-called control cycles are employed to update the spatial field of the strain amplitude and to compute the energy capacity and efficiency of the GGES system.

In the (B) explicit calculation phase, the cumulative behavior of sand under high-cyclic loading with small strain amplitudes $\left(\epsilon^{\text{ampl}} < 10^{-3}\right)$ is modeled using the barotropic, elasto-plastic HCA model [22]. This constitutive model captures only the general strain and/or stress accumulation trend but does not track the detailed behavior of each individual cycle (Fig. 4). With the rate per cycle $d \sqcup / dN = \hat{\sqcup}$, the HCA model is expressed as

$$\hat{\boldsymbol{\sigma}} = \mathsf{E} : \left(\hat{\boldsymbol{\epsilon}} - \hat{\boldsymbol{\epsilon}}^{\text{acc}} - \hat{\boldsymbol{\epsilon}}^{\text{pl}}\right) \tag{5}$$

with the stress rate $\hat{\boldsymbol{\sigma}}$, the strain rate $\hat{\boldsymbol{\epsilon}}$, the plastic strain rate $\hat{\boldsymbol{\epsilon}}^{\text{pl}}$, the accumulated strain rate $\hat{\boldsymbol{\epsilon}}^{\text{acc}}$, and the barotropic elastic stiffness E [22]. In addition to the effective Cauchy stress $\boldsymbol{\sigma}$ and the void ratio e, the HCA model also includes a further scalar state variable called cyclic preloading g^A. The accumulation rate

$$\hat{\boldsymbol{\epsilon}}^{\text{acc}} = \boldsymbol{m} \cdot \hat{\epsilon}^{\text{acc}} = \boldsymbol{m} \cdot f_{\text{ampl}} \hat{f}_N f_e f_p f_Y f_\pi \tag{6}$$

can be calculated using the flow rule $\boldsymbol{m}$ (direction of accumulation) of the modified cam clay model. Six empirical factors (f_{ampl}, $\hat{f}_N$, f_e, f_p, f_Y, f_π) affect the intensity of the strain accumulation $\hat{\epsilon}^{\text{acc}}$. These account for various influences such as the strain amplitude (f_{ampl}), the cyclic preloading ($\hat{f}_N$), the mean effective pressure (f_p), the stress ratio (f_Y), the void ratio (f_e), and the polarization changes (f_π) on the accumulation effects. The HCA model, developed based on comprehensive experimental high-cycle tests [25], is discussed in detail along with its parameter determination in the literature [22,25].

3. Parameter calibration

The overall GGES system is analyzed in this study based on the simplified assumption that the overburden soil consists of Karlsruhe fine sand (KFS), which is a well-known material that has been extensively tested experimentally in the literature [25,30–32]. Numerical simulations of KFS using both the HCA model and the HP+IS model have also been documented [26,33,34]. However, these experimental and numerical studies address problems located at relatively shallow depths, which results in a relatively low mean effective pressure in the soil. In contrast, the GGES system operates at much greater depths and the overburden height can be several hundred meters. As a result, the stress–strain behavior of the soil becomes relevant over a much wider range of mean effective pressures. Furthermore, due to the large radial dimensions of the GGES system, oedometric conditions become particularly relevant. Before presenting the numerical analyses in the following sections, the constitutive models and their parameter sets must first be calibrated based on laboratory tests.

To evaluate the oedometric stiffness of KFS with the implicit constitutive model under both monotonic and cyclic loading, oedometric compression tests ($\epsilon_r = 0$) were performed. These tests involved an initial loading to $\sigma_a = -1700$ kPa, followed by 10 un- and reloading cycles with $\Delta\sigma_a = 500$ kPa. The tests were conducted on a medium dense sample with an initial relative density of $I_{D0} \approx 0.4$ and a dense sample with $I_{D0} \approx 1.0$. The relative density is defined as

$$I_D = \frac{e_{\max} - e}{e_{\max} - e_{\min}} \overset{\text{HP+IS}}{=} \frac{e_{c0} - e}{e_{c0} - e_{d0}} \ . \tag{7}$$

Note that throughout this paper, the mechanical sign convention is used, where tensile stress and expansive strain are positive.

The experimental results are presented in Fig. 5 and are used to adjust the constitutive parameters for the HP+IS for KFS, already calibrated in [25], to account for higher pressure conditions. The results of the element test simulations, performed using the modified parameter set provided in Table 1, are also shown in Fig. 5. These

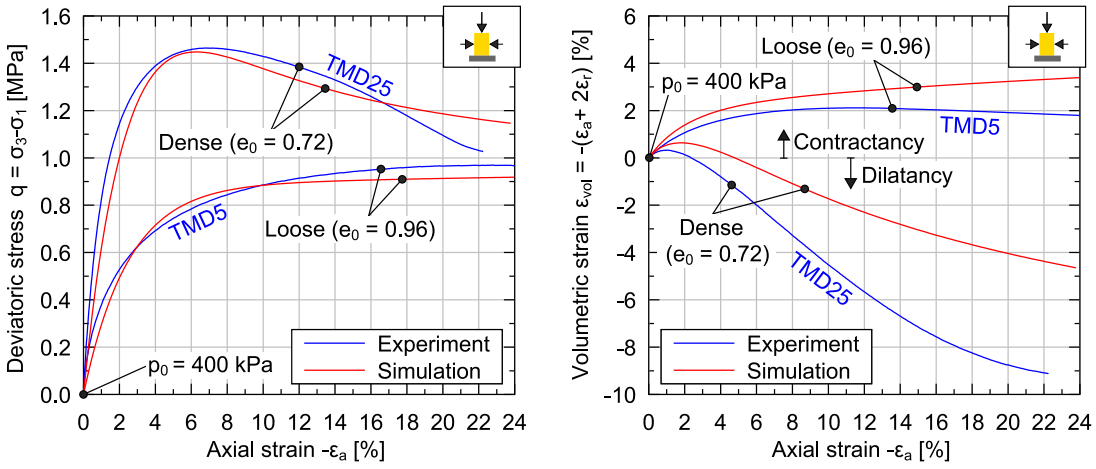

(a) (b)

Fig. 6. Drained triaxial compression tests on Karlsruhe fine sand (KFS) on loose and dense samples with an isotropic initial stress $p_0 = 400$ kPa: experimental results from [32] (blue) versus simulations using HP+IS (red).

Table 1
Modified parameter set from [25] of HP + IS for Karlsruhe fine sand (KFS).

φ_c [°]	e_{i0} [–]	e_{c0} [–]	e_{d0} [–]	h_s [MPa]	n [–]	α [–]	β [–]	R [–]	m_R [–]	m_T [–]	β_R [–]	χ [–]
33.1	1.212	1.054	0.677	1600	0.25	0.19	2.5	10^{-4}	1.3	1.15	0.1	6.0

simulations were conducted with the freely available program code IncrementalDriver [35] and an Abaqus umat.for subroutine developed by Prof. A. Niemunis. An isotropic stress state of $\sigma_{a0} = \sigma_{r0} = -25$ kPa and the corresponding void ratio e_0 measured in the test is initialized in the simulations. Additionally, the initial intergranular strain is fully mobilized in the vertical direction. The results clearly show that the dense sample exhibits significantly higher oedometric stiffness compared to the loose sample, with increased stiffness with increased axial stress (pressure). Moreover, the soil becomes stiffer during un- and reloading, in contrast to the initial virgin loading. The element test simulations, using the adjusted parameter set for the HP+IS from Table 1, reproduce the observed nonlinear soil behavior qualitatively and quantitatively. Due to the high effective pressure, the material parameters controlling the stiffness increase upon a reversal of loading in the intergranular strain concept, namely m_R and m_T, were significantly reduced compared to the provided parameter set from [25]. This observation is consistent with the results from [36].

Drained triaxial compression tests on a dense sample ($I_{D0} = 0.89$) and a loose sample ($I_{D0} = 0.25$), with an initial effective isotropic stress of $p_0 = -(\sigma_{a0} + 2\sigma_{r0})/3 = 400$ kPa, as reported in [25] (TMD25 and TMD5), are used for further parameter validation. Fig. 6 presents the experimental data and the simulation results. The dense sample shows a pronounced peak strength, represented by the maximum deviatoric stress ($q = \sigma_r - \sigma_a$), as well as a pronounced dilatancy, defined as an increase in volume due to shear strain. In contrast, the loose sample exhibits no peak strength and shows purely contractive behavior throughout the test. The element test simulations reveal a good correlation with the experimental data. However, the underestimated dilatancy of the dense sample (Fig. 6b) highlights a well-known limitation of the hypoplasticity after von Wolffersdorff [25,37]. Note that more recent constitutive models [37–39] can address the shortcomings of the implicit model. Nevertheless, these issues are of minor relevance for the GGES analysis.

Further parameters are required to describe the accumulative behavior in the explicit HCA model. These HCA parameters for KFS have been calibrated based on an extensive experimental database [25]. To address the wide range of effective pressures acting in a GGES system,

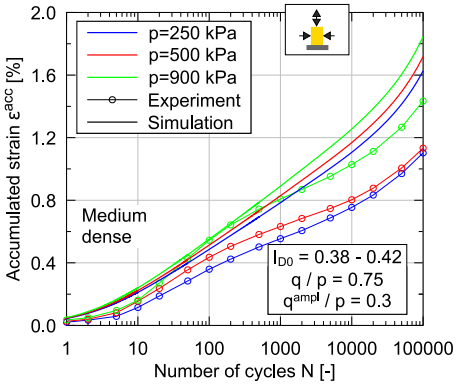

Fig. 7. Drained cyclic triaxial tests on Karlsruhe fine sand (KFS) with different mean effective pressures: experimental results from [30] versus simulations using the HCA model.

Table 2
Modified parameter set from [25] of the HCA model for Karlsruhe fine sand (KFS).

C_{ampl} [–]	C_e [–]	C_p [–]	C_Y [–]	C_{N1} [10^{-4}]	C_{N2} [–]	C_{N3} [10^{-5}]
1.33	0.60	0.09	1.68	2.95	0.41	1.90

the parameter C_p describing the dependence of the accumulation rate on the mean effective pressure is adjusted in this study. C_p was previously calibrated for a pressure range of 50 kPa $< p <$ 300 kPa [25]. For higher pressures in the range of 200 kPa $< p <$ 900 kPa a more recent calibration resulted in an updated value of $C_p = 0.09$ for KFS [30]. The HCA parameters used in the following simulations are summarized in Table 2.

Fig. 7 presents experimental results of drained high-cycle triaxial tests conducted on medium-dense samples ($I_{D0} \approx 0.4$) with varying average mean effective pressures $p^{av} = p$ and a constant average stress ratio of $q/p = 0.75$ from [30]. An identical stress amplitude ratio q^{ampl}/p was applied in these tests, which resulted in varying

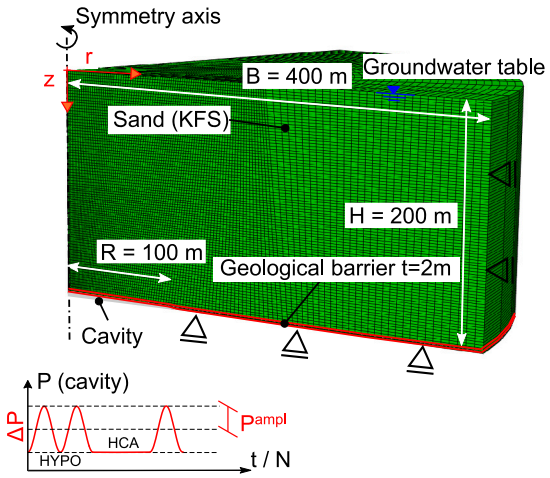

Fig. 8. Schematic illustration of the axisymmetric boundary value problem of the GGES system using a simplified pressure boundary condition to simulate the cavity.

strain amplitudes ϵ^{ampl}. The accumulated strain, defined as $\epsilon^{\text{acc}} = \|\epsilon^{\text{acc}}\|$, exhibits a strongly non-linear increase as the number of cycles N increases. The tests reveal similar accumulation behavior across a wide pressure range (250 kPa $< p <$ 900 kPa). Numerical simulations using the HCA model successfully replicate both the qualitative and quantitative trends observed in the experimental data, highlighting the model's ability to capture accumulation effects under cyclic loading. The HCA model slightly overestimates accumulation with the chosen parameters.

The subsequent numerical analyses of the GGES concept are intended as a simplified and qualitative investigation. In this regard, the model prediction appears to be conservative. Therefore, further refinement of the parameter calibration is neither necessary nor justified.

4. Boundary value problem

The GGES system is analyzed solving an axisymmetric boundary value problem with a radius of $B = 400$ m (Fig. 8). A system with an overburden height of $H = 200$ m is modeled. For simplicity, the geological barrier is assumed to be linear elastic ($E = 500$ MPa and $\nu = 0.25$) representing the lowest 2 m of the overburden directly above the cavity. The sand is considered to be fully saturated with the groundwater level positioned at the ground surface. The latter represents the only hydraulically permeable boundary in the model, where a pore fluid pressure of $p_f = 0$ is applied. The bulk modulus of the pore fluid is assumed to be $K_f = 2.2$ GPa. Assuming that the geological barrier is almost impermeable, the pressure in the cavity is equivalent to the total overburden pressure. The coupled hydro-mechanical analysis (with the differentiation into effective and total stress in the sense of Terzaghi) is performed only within the sand layer, whereas a purely mechanical analysis, based on total stress, is conducted in the geological barrier.

For the sake of simplicity, the double membrane described in Section 1 is not explicitly modeled, since its comparatively low stiffness does not significantly affect the overall mechanical behavior of the GGES system. The cavity radius is $R = 100$ m, and the cavity itself is modeled using a simplified prescribed pressure boundary condition, which simulates the pressure applied to the soil by the pressurized fluid within the cavity. As fluid is pumped into the cavity both the fluid pressure P and the cavity volume V increase. Starting from the geostatic pressure, the cavity pressure increases during the charging phase of an energy storage cycle by a pressure difference of $\Delta P = 2P^{\text{ampl}}$ and returns to the initial geostatic pressure at the end of the discharging phase. As it is shown schematically in Fig. 8, ΔP describes the span between the maximum and the minimum fluid pressure during an energy storage cycle. The resulting displacement of the cavity wall is integrated numerically in a post-processing step to calculate the corresponding cavity volume. An alternative approach to model the cavity using a so-called surface-based fluid cavity in Abaqus, which directly prescribes the cavity volume, can be found in [15,26]. The equivalence of both approaches has been verified under dry conditions. However, the fluid cavity approach cannot be applied for saturated soils due to the limitations of Abaqus.

Table 3
Steps of the HCA calculation for the analyses of the GGES system.

Number	Step	Calculation phase	Cycle
1	Geostatic	Implicit	–
2	Irregular cycle	Implicit	0[a]
3	1. Regular cycle	Implicit	1
4	1. HCA-phase	Explicit	2–100
5	1. Control cycle	Implicit	101
6	2. HCA-phase	Explicit	102–1000
7	2. Control cycle	Implicit	1001
8	3. HCA-phase	Explicit	1002–10 000
9	3. Control cycle	Implicit	10 001
10	4. HCA-phase	Explicit	10 002–20 000
11	4. Control cycle	Implicit	20 001
12	5. HCA-phase	Explicit	20 002–40 000
13	5. Control cycle	Implicit	40 001

[a] The irregular cycle leads to large deformations.

Fig. 8 schematically illustrates the additional mechanical boundary conditions of the considered boundary value problem. The outer boundary at $r = B = 400$ m is fixed in the radial direction, while no vertical displacements are allowed at the lower boundary at $z = H = 200$ m next to the cavity with $r > R = 100$ m. Additionally, shear stresses are not permitted at any boundary of the axisymmetric model and the applied stress at the ground surface is set to zero.

The terms 'dense' and 'loose', as usually used to describe the mechanical behavior of granular soil, depend not only on the current density (void ratio), as described by the relative density according to Eq. (7), but also on the current pressure. Therefore, Eq. (7) can be extended and a pressure-dependent relative density

$$I_{d0} = \frac{e_c(p) - e}{e_c(p) - e_d(p)} , \tag{8}$$

with pressure-dependent limit void ratios $e_c(p)$ and $e_d(p)$, can be defined. To initialize a constant pressure-dependent relative density, the initialized void ratio e_0 decreases with increasing mean effective pressure, respectively with increasing depth, according to the compression law [40]:

$$e_0(p) = e_0(p=0) \exp\left[-\left(\frac{3p}{h_s}\right)^n\right] . \tag{9}$$

For simplicity, the weight of the soil is assumed to be constant with depth, meaning the initial stress increases linearly with depth. An initial lateral pressure coefficient of $K_0 = 0.5$ is assumed in all calculations for the initial stress field. The initial intergranular strain $\boldsymbol{h}_0$ is assumed to be fully mobilized in vertical direction, with $h_{v0} = -R$ and no cyclic preloading is initialized ($g_0^A = 0$).

As explained in Section 2, the implicit and explicit phases alternate during an HCA calculation. The calculation steps involved in the simulations are listed in Table 3. It is important to note that changes in the shared state variables (such as the effective stress and the void ratio) of the implicit and the explicit model occur in both the explicit and implicit phases. However, non-shared state variables (such as the intergranular strain $\boldsymbol{h}$ and the cyclic preloading g^A) changes only during the corresponding simulation phase.

A specific detail in the application of the HCA model for GGES analysis should be highlighted. Instead of applying the cyclic loading in the (A) implicit phase centered around an average value and calculating the

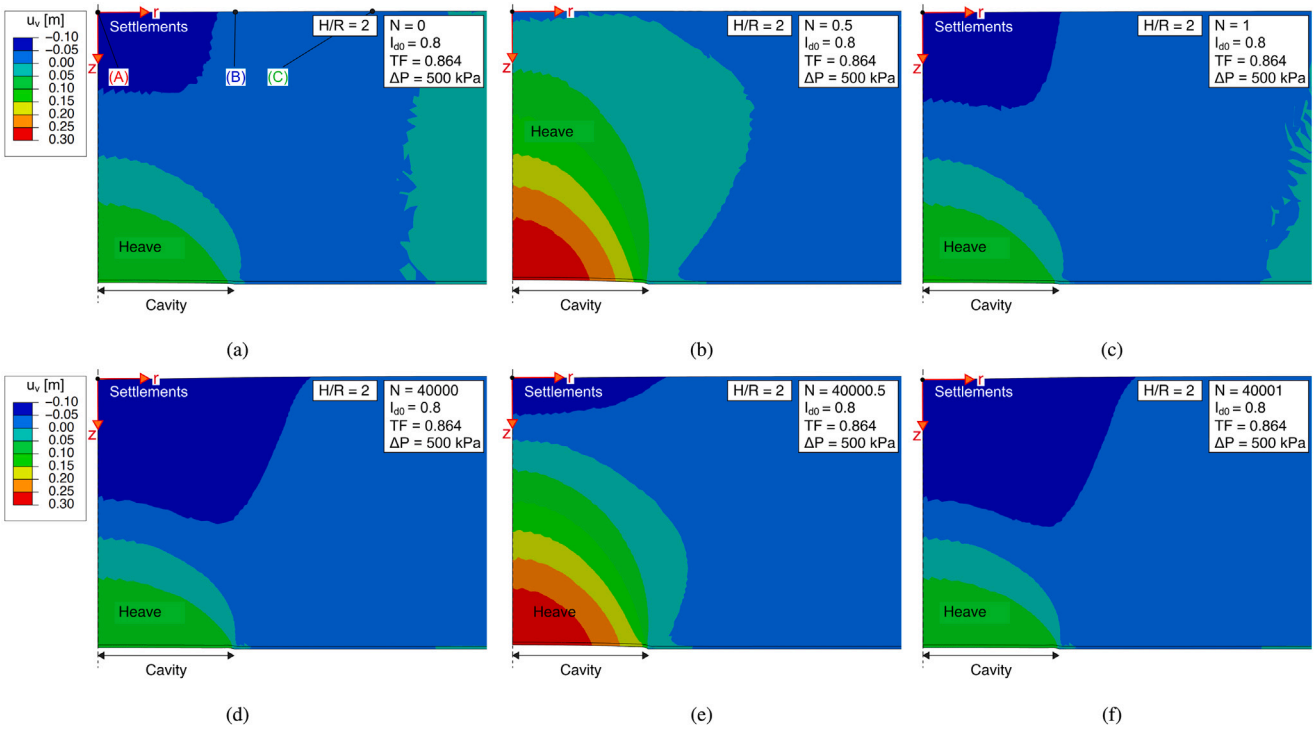

Fig. 9. Total vertical displacements u_v at (a) the beginning, (b) the peak, and (c) the end of the 1st and at (d) the beginning, (e) the peak, and (f) the end of the 40 001st regular energy storage cycle N.

accumulation in the (B) explicit phase based on this average value [22], a different approach is more practical for GGES analysis. As schematically shown in Fig. 4, the original HCA approach would use the average value of the cavity pressure. However, in the present GGES analysis, it is more practical to calculate the accumulation and cyclic loading starting from the minimum value of the cavity pressure, as illustrated in Fig. 8. Although this approach deviates from the original HCA concept, it provides almost identical results for the analyzed problem (deviations of less than 1%). The benefit of this modified application of the HCA model lies in a significantly simplified interpretation of the simulations.

A physical time dependency arises in the considered problem due to the interaction between (I) the loading frequency f (i.e., the frequency of energy storage) or the corresponding periodic time $T = 1/f$ (i.e., the duration of the energy storage cycle), and (II) the consolidation processes, which depend on the permeability k and the geometry of the GGES system (drainage path). These two effects can be combined by introducing a dimensionless time factor TF:

$$TF = T\ [\mathrm{s}] \cdot k\ [\mathrm{m/s}] \ /\ 1\ [\mathrm{m}]\ . \tag{10}$$

Thus, quasi-static simulations with the same time factor TF and identical geometry can be interpreted for various combinations of periodic time T and permeability k. For example, a time factor of $TF = 0.864$ corresponds to a periodic time $T = 1$ day and a permeability of $k = 10^{-5}$ m/s, or alternatively, a periodic time $T = 100$ days and a permeability of $k = 10^{-7}$ m/s. Similarly, a time factor of $TF = 86.4$ corresponds for example to a periodic time $T = 100$ days and a permeability of $k = 10^{-5}$ m/s.

The practical use of the GGES will be primarily driven by economic interests, which will result in non-uniform periodic times and non-constant pressure differences ΔP in real-world applications. From a mechanical perspective, scenarios with shorter periodic times and smaller pressure differences are safer, as these variants lead to reduced changes in the pore fluid pressure and decreased accumulative effects. In any case, the loading process is slow enough to neglect dynamic effects.

The numerical model, solved in Abaqus, consists of the sand layer discretized using 4128 reduced integrated elements (CAX4RP) to reduce unintended self-stresses during the analyses [41]. The geological barrier is modeled using 2200 CAX4R elements. Comparative calculations with a finer mesh confirmed that the current mesh refinement is sufficient for the problem being analyzed.

5. Numerical results

5.1. Reference variant

A reference variant is analyzed with an initial relative density of $I_{d0} = 0.8$ (dense sand), a pressure difference of $\Delta P = 500$ kPa, and a time factor of $TF = 0.864$. The geometric ratio is set to $H/R = 200/100 = 2$. Fig. 9 illustrates the total vertical displacements u_v at the beginning, peak, and end of both the 1st and the 40 001st regular energy storage cycle N. Corresponding total radial displacements u_r are presented in Fig. 10. The displacements are scaled by a factor of 10. Additionally, Fig. 11 provides detailed insights into the total displacements within three horizontal cross-sections (ground surface ($z = 0$), middle ($z = H/2 = 100$ m), and bottom ($z = H = 200$ m) of the model) and two vertical cross-sections at $r = R = 100$ m and $r = 2R = 200$ m.

The first irregular cycle (not shown) causes an irreversible cavity expansion, settlements at the ground surface, and small radial displacements (Fig. 9a and 10a). This deformed state of the GGES serves as the reference for the subsequent regular energy storage cycles. Due to the significant irreversible deformations caused during the first irregular cycle, the ground surface remains consistently lower than its original elevation in all cavity filling stages of the regular cycles. The settlements at the ground surface are most pronounced in a fully discharged system, forming a shallow basin as illustrated in Figs. 9c, d and f and 11a. Within each regular energy storage cycle, the overburden soil undergoes lifting and lowering as shown in Figs. 9b and e and 11a. By the end of a regular cycle, the system nearly returns to its state at the beginning of that cycle. The difference between these two states

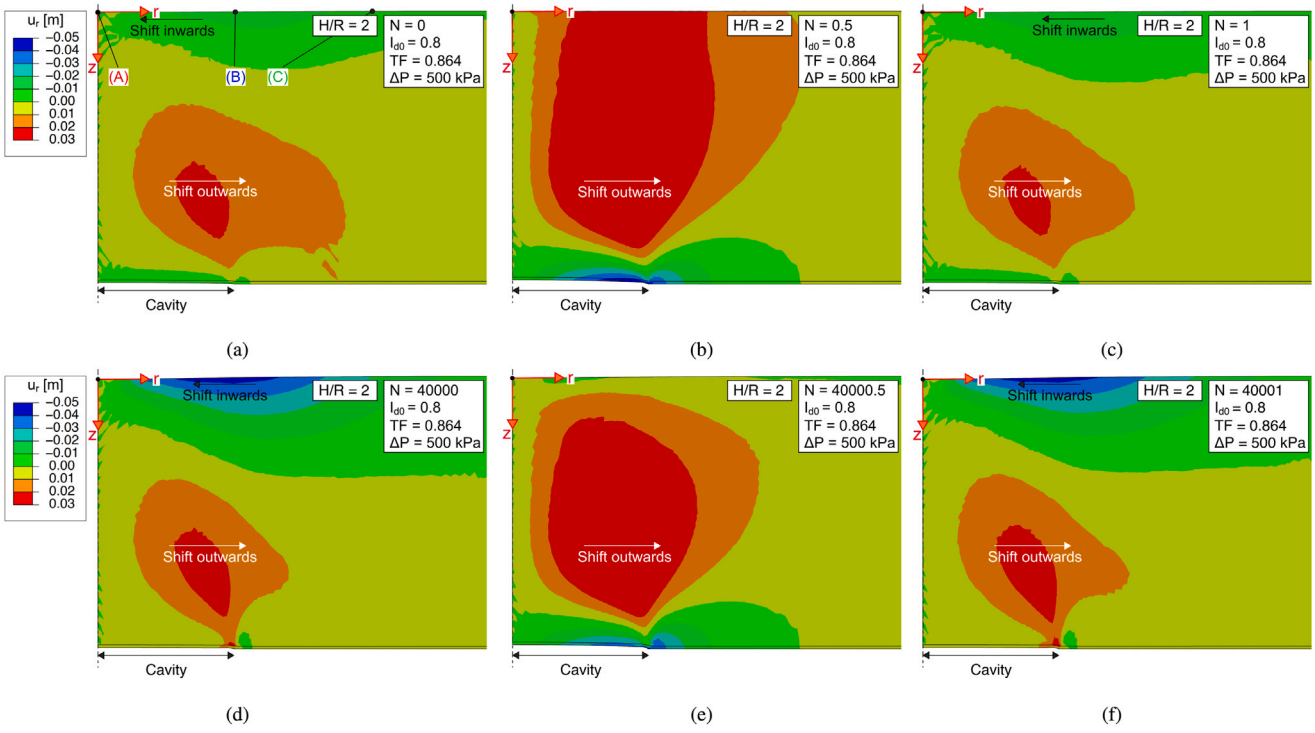

Fig. 10. Total radial displacements u_r at (a) the beginning, (b) the peak, and (c) the end of the 1st and at (d) the beginning, (e) the peak, and (f) the end of the 40 001st regular energy storage cycle N.

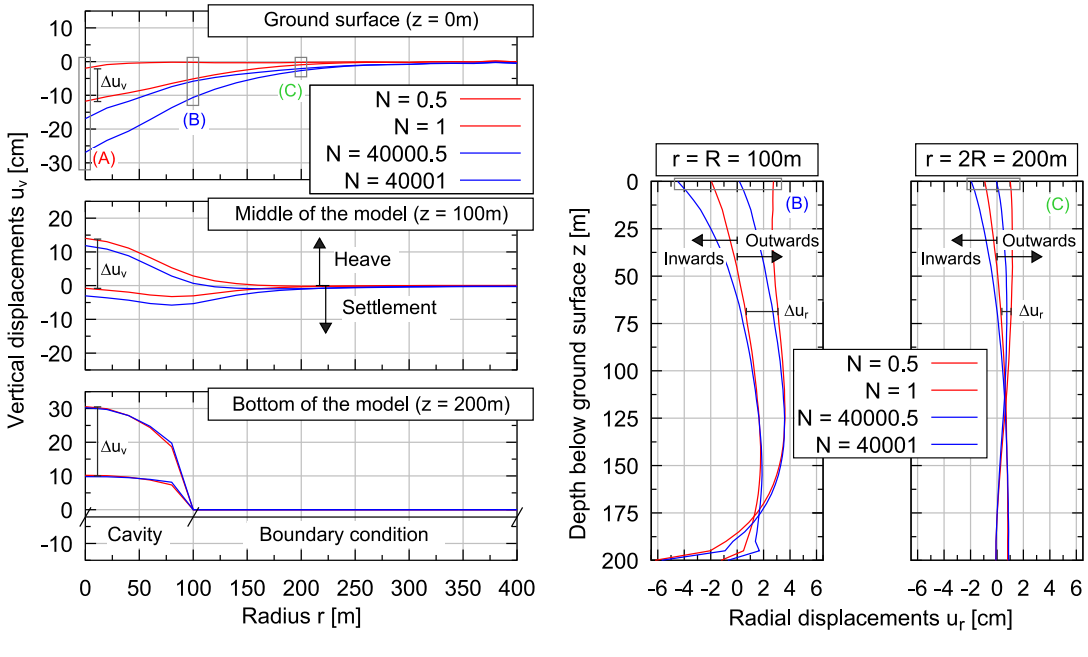

Fig. 11. Total displacements in the 1st and in the 40 001st regular energy storage cycle N in (a) vertical direction u_v in three horizontal cross-sections and (b) in radial direction u_r in two vertical cross-sections.

represents the cumulative effect, which is more prominent in the first cycle compared to the 40 001st cycle. This can be by seen comparing Fig. 9a and c for the first cycle and Fig. 9d and f for the 40 001st cycle.

As shown in Figs. 9 and 11a, the maximum vertical heave within a regular cycle (incremental displacement) of approximately $\Delta u_v \approx 0.2\,\text{m} = H/1000$ occurs directly above the center of the cavity ($r = 0$) at $z = H$ in the maximum filling stage. This vertical displacement within each regular cycle decreases towards the ground surface, reaching approximately $\Delta u_v \approx 0.1\,\text{m} = H/2000$ at $z = 0$ (Point A at $r = 0$).

Filling the cavity results additionally in outward radial displacements, with a maximum incremental value of approximately $\Delta u_r \approx 0.05\,\text{m} = R/2000$ at the ground surface at a radius of $r = R$ (Point B), as it can be seen in Figs. 10 and 11b. With increasing radial distance, the horizontal displacements decrease, and due to the symmetry condition,

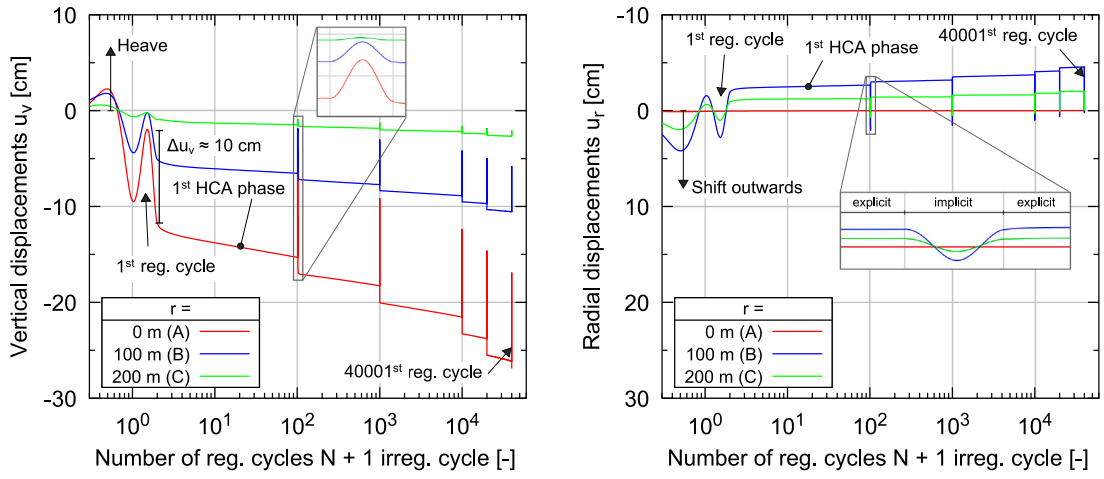

(a) (b)

Fig. 12. Total displacements at the ground surface as a function of the number of energy storage cycles N in (a) vertical direction u_v and (b) in radial direction u_r for three different points A ($r = 0$), B ($r = R = 100$ m) and C ($r = 2R = 200$ m).

$u_r = 0$ applies at $r = 0$. These radial displacements are considerably smaller than the vertical ones.

A comparison between the deformations after the 1st and the 40 001st cycle reveals accumulative deformations. However, these do not qualitatively impact the overall behavior of the GGES system.

The deformations at the ground surface are of great interest. Fig. 12 illustrates the total vertical and radial displacements at three specific points on the ground surface ($z = 0$): (A) directly at the center of the model ($r = 0$), (B) above the cavity edge ($r = R = 100$ m), and (C) at twice the cavity radius ($r = 2R = 200$ m) (see Figs. 11 and 9a). These displacements are shown as a function of the number of cycles N for both implicit and explicit calculation phases in Fig. 12. For the explicitly calculated cycles, the lifting and lowering (or outward and inward movements) within a single energy storage cycle are not simulated, as these phases primarily capture the accumulative deformation trends.

Within each energy storage cycle, the ground surface at Point A ($r = 0$) is lifted and lowered by approximately $\Delta u_v \approx 0.1\,\text{m} = H/2000$, as already discussed and shown in Fig. 12a. At Point B, directly above the cavity edge ($r = R = 100$ m), the vertical displacements are reduced to about half of this value. At Point C, located at twice the radius of the cavity $r = 2R = 200$ m, the vertical displacements at the ground surface are negligible. In addition to these within-cycle displacements, cyclic deformations result in cumulative settlements over the number of cycles. After 40 000 regular energy storage cycles, the accumulated settlement at Point A is approximately $u_v^{\text{acc}} \approx 25$ cm. At Point B, the cumulative settlement is about half of this value. At Point C, the cumulative settlements diminish further, becoming negligible at approximately $u_v^{\text{acc}} \approx 2.5$ cm.

The radial displacements at the ground surface, as shown in Fig. 12b, are notably smaller than the vertical displacements. Due to the axisymmetric conditions of the system, Point A remains fixed in the radial direction. In contrast, Point B exhibits approximately twice the incremental radial displacement ($\Delta u_r \approx 0.05\,\text{m} = R/2000$) of Point C ($\Delta u_r \approx 0.025\,\text{m} = R/4000$). An accumulative inward radial movement is observed. This inward accumulation is most pronounced at Point B but remains relatively small in magnitude, with a cumulative radial settlement of approximately ($u_r^{\text{acc}} \approx 4.5$ cm after 40 001 cycles).

Based on these results, the inclination of the ground surface after 40 000 cycles can be estimated as $\Delta s/L \approx 0.225/200 \approx 0.0011 < 1/750$. With this inclination, no damage to ordinary buildings is expected [42]. Even during operation, no larger inclinations occur for the case under consideration. Furthermore, the documented relatively small deformations do not indicate any risk of damage to the mechanical equipment of the GGES itself. However, the deformations and inclinations strongly depend on the applied pressure and/or volume amplitudes during operation. Therefore, the surface above a GGES system should preferably be used for agriculture or energy production (e.g., photovoltaic).

The most important factor for calculating these accumulative effects using the HCA model is the scalar strain amplitude $\varepsilon^{\text{ampl}}$, as discussed in Section 2. The spatial distribution of this scalar quantity is shown in Fig. 13 for the 1st and 5th HCA phases. Within each HCA phase, this field is assumed to remain constant and is updated during the control cycles occurring between the HCA phases. The largest strain amplitudes appear in the area above the edge of the cavity at $z = H$ and $r = R$ and at the symmetry axis at the ground surface at $z = 0$ and $r = 0$. The calibration limit of the HCA model, which is at $\varepsilon^{\text{ampl}} = 10^{-3}$ [22], is only reached and slightly exceeded in a small area directly above the cavity edge. Despite the large displacements occurring at the center of the model above the cavity ($z = H$ and $r = 0$), as illustrated in Figs. 9 and 10, the incremental strain and, consequently, the strain amplitude observed during a regular energy storage cycle are relatively small. Moreover, the spatial distribution of the strain amplitude does not change significantly between the different HCA phases.

In general, changes in pore fluid pressure in saturated soil can result from both isotropic compression/extension and shearing due to dilatancy/contractancy. However, in the presented reference variant, these changes are negligibly small. A further increase in the time factor TF would lead to even smaller changes in the pore fluid pressure. Smaller time factors are not considered due to the expected real-life energy storage duration [1]. The influence of the permeability on the overall mechanical behavior of a GGES system can therefore be neglected, although it is essential to consider fully saturated conditions.

Cyclic deformations of the soil typically lead to two effects: (I) cumulative compaction (densification) and (II) cumulative stress relaxation. These tendencies become more pronounced with greater strain amplitudes and both effects occur in the GGES. Fig. 14 illustrates the spatial distribution of the void ratio e (densification) and the mean effective pressure $p = -\text{tr}(\boldsymbol{\sigma})/3$ after the 40 001st energy storage cycle. A localized reduction of the void ratio can be observed directly above the cavity. Notably, the initial void ratio decreases with depth to ensure a constant relative initial density I_{d0} according to Eq. (9). At the edge of the cavity ($z = H$ and $r = R$), where the strain amplitude is largest, the mean effective pressure is reduced by approximately 50 %. However, it should be emphasized that liquefaction effects ($p \approx 0$) due to cyclic deformation do not occur.

An anisotropic initial stress state with a lateral pressure coefficient of $K_0 = 0.5$ has been assumed. In addition to pressure changes,

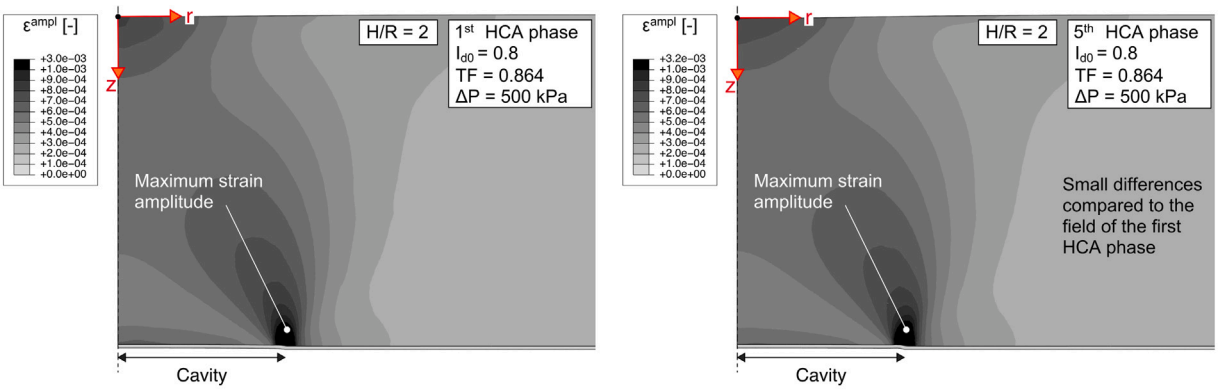

Fig. 13. Spatial distribution of the scalar strain amplitude ϵ^{ampl} in the (a) 1st and the (b) 5th HCA phase.

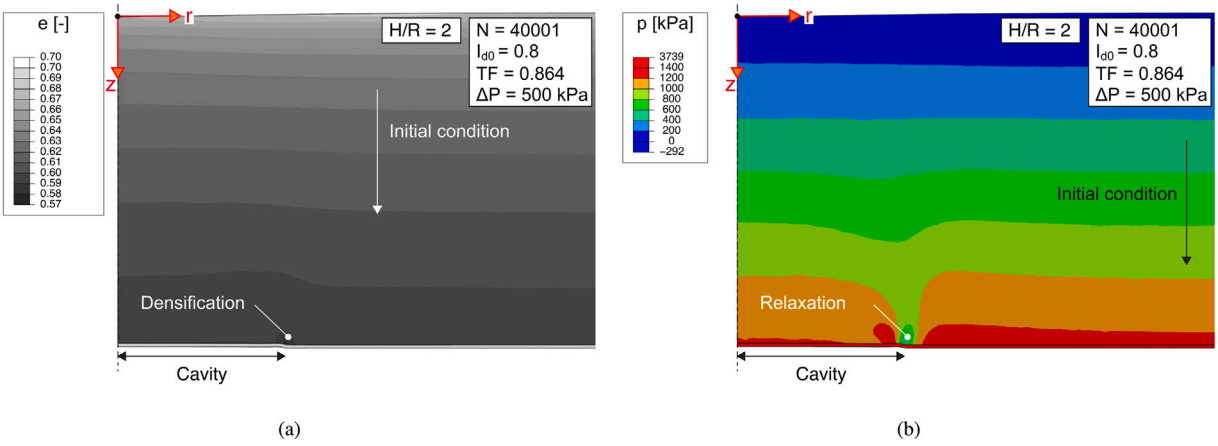

Fig. 14. Spatial distribution of (a) the void ratio e and (b) the mean effective pressure $p = -\mathrm{tr}(\sigma)/3$ after 40 001 energy storage cycles.

cyclic deformations lead to changes in the stress ratio (not shown graphically). The stress ratio is significantly reduced in the main part of the soil mass, shifting the stress state from an initially anisotropic condition toward a more isotropic stress state far from failure. Only near the cavity edge ($z = H$ and $r = R$) does the stress ratio increase slightly. From this, it can be concluded that soil strength has a negligible influence on the overall performance of the GGES system.

The energy capacity and the efficiency of the energy storage system can be calculated using the pressure P and the volume V of the fluid within the cavity. Energy capacity is further defined as the output energy E_{out} per energy storage cycle, while the efficiency η can be determined according to Eq. (3). This soil mechanical efficiency only considers the energy losses within the soil resulting from its non-fully elastic (reversible) mechanical behavior. Both the energy capacity and efficiency can only be determined in implicitly calculated cycles. The fluid pressure P is known directly from the prescribed pressure boundary condition and the volume of the cavity V is calculated numerically by considering the vertical displacements of the affected nodes during a post-processing step. For simplicity, radial displacements of these nodes are neglected.

The resulting pressure-volume curve for the implicitly calculated cycles of the reference variant is shown in Fig. 15. For this variant, a capacity of 4705.3 kWh with a soil mechanical efficiency of $\eta = 97.3\%$ is achieved in the first regular energy storage cycle and a capacity of 4786.0 kWh with a soil mechanical efficiency of $\eta = 97.7\%$ is achieved in the 40 001st energy storage cycle.

Notably, the cyclic deformation leads to an improvement in both the capacity and efficiency of the GGES system as the number of energy storage cycles increases. In the reference variant presented, the capacity increases by approximately 1.7% after 40 000 energy storage cycles. Although these positive aging effects are relatively small, this characteristic behavior distinguishes the GGES system from most energy storage technologies. Unlike many other energy storage systems [1], the GGES system does not exhibit any degradation in energy storage capacity or efficiency over time. This positive behavior is attributed to a decrease in the accumulation rate of stresses and strains with an increasing number of cycles, as well as the overall small strain amplitudes within each energy storage cycle and the nearly constant strain amplitude in the soil over multiple cycles. Compared to previous numerical analyses of GGES and UPHES systems [15,26], this study considers a numerical model with a prescribed pressure amplitude in the cavity. In practical applications, controlling the pressure appears to be more effective than controlling the volume of the cavity. As shown in Figs. 11 and 15, this results in a slight cumulative increase in the cavity volume (cyclic cavity expansion) and in the volume amplitude within each cycle over the system's operation time. In the examined case, the volume amplitude between the 1st and the 40 001st regular cycle increases slightly by about 1.7%, while the overall cavity volume increases by approximately 9.8%. This expansion is not expected to cause any practical issues.

The energetic analyses are based on the pressure measured directly in the cavity. As described in Section 1, the effective usable pressure of the system depends on the location of the powerhouse, the local topography, and the groundwater level. In the presented scenario with a horizontal ground surface, fully saturated soil at the specified soil density, and a fluid weight of $\gamma_{Fluid} = 10$ kN/m^3 in the GGES system,

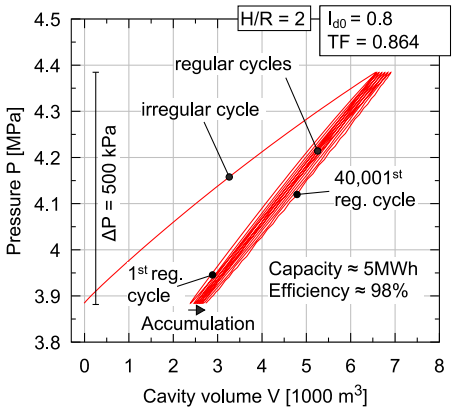

Fig. 15. Pressure of the fluid in the cavity P as a function of the volume of the cavity V ($P-V$ curve).

the practically usable energy capacity is approximately 2.5 MWh, and the soil mechanical efficiency is $\eta \approx 97\%$. Note again that the stated efficiency includes only energy losses within the soil.

In addition to the calculated negligible energy losses caused by the soil's mechanical behavior in a GGES, energy losses due to pipe friction and energy transition will also occur in a real GGES. These energy losses are assumed to be comparable to those in a conventional pumped hydro energy storage (PHES) plant [7,9] and the overall efficiency of a GGES system is expected to be approximately 80%.

Instead of the complex numerical simulation of the GGES system and the subsequent post-processing, the energy E_{out} can also be determined as a function of the pumped-in volume ΔV per storage cycle, using the specific weight of the saturated overburden soil γ_r, the radius of the cavity R, and the overburden height H:

$$E_{\text{out}} = H\gamma_r \Delta V = H\pi R^2 \gamma_r \Delta V / \pi R^2 = V_{\text{Overburden}} \gamma_r \Delta h \ . \tag{11}$$

Thus, $\Delta h = \Delta V / A$ represents the average incremental heave of the soil directly above the cavity. For the presented variant ($I_{d0} = 0.8$, $\Delta P = 500$ kPa, $TF = 0.864$), this simplified approach results in a capacity of 4530 kWh in the first regular energy storage cycle and a capacity of 4590 kWh in the 40 001st regular energy storage cycle. This simple formula shows deviations of less than 5% compared to the complex numerical analysis of the GGES system presented in this paper. It can be concluded that Eq. (11) is suitable for the preliminary design of GGES systems. However, for larger values of Δh, Eq. (11) may yield large deviations from the numerical analysis.

5.2. Parameter study

A parameter study of the GGES system is conducted to investigate the influence of the following factors: (I) the applied pressure difference in the cavity during the energy storage cycles ΔP, (II) the time factor TF according to Eq. (10), (III) the initial relative density I_{d0}, and (IV) the geometric ratio of the overburden height H divided by the cavity radius R, denoted as H/R.

The capacity and efficiency of the 40 001st energy storage cycle of the GGES are analyzed as a function of the applied pressure difference for initial relative densities of $I_{d0} = 0.8$ and $I_{d0} = 0.4$ in Fig. 16. Time factors of $TF = 0.864$ and $TF = 86.4$ are considered. In addition to the variants with $H/R = 2$, a geometric ratio of $H/R = 4$ is examined. The number of elements was increased for the latter simulations. For all variants, the cavity radius of $R = 100$ m was considered. The same results are shown in Fig. 17 as a function of the mean cavity increase $\Delta h = \Delta V / A$, with a normalized capacity based on the volume of the overburden soil. Fig. 17 also includes the capacity calculated using the simplified Eq. (11).

It can be observed that an increased pressure difference ΔP increases the capacity but decreases the efficiency of the GGES system. The relative initial density has a significant effect on the pressure difference required to achieve a certain capacity and a certain mean cavity increase, as shown in Fig. 16a and b. Additionally, Fig. 17a and b reveals that the energy losses for the same mean cavity increase are greater, and the capacity is smaller in loose soil compared to dense soil, due to the overall decrease in soil density. However, the differences are small. An increase in the time factor has only a minor effect on the overall behavior, as the pore pressure evolution remains small across all variants. Both capacity and efficiency increase slightly, as the changes in pore fluid pressure are further reduced with an increased time factor TF. The effect of permeability on the overall behavior of a GGES system can be neglected.

Doubling the overburden height doubles the overburden pressure. Calculations with larger pressure differences are therefore needed to achieve comparable volume differences ΔV in the cavity. As a result, approximately twice the capacity can be achieved with comparable efficiency, as shown in Figs. 16a and 17d. It should be emphasized that the efficiency and the capacity of the overall system mainly depend on the mean cavity increase ($\Delta h = \Delta V / A$), while other geometric ratios, such as $\Delta h / H$, are not decisive. Fig. 17 demonstrates additionally that the simplified Eq. (11) can be used highly effectively to determine the capacity of the GGES system as long as the soil mechanical efficiency of the system is greater than $\eta \approx 95\%$.

To evaluate the influence of the geometric ratio H/R in detail, Fig. 18 illustrates the spatial distribution of the strain amplitude $\varepsilon^{\text{ampl}}$ for $H/R = 4$. The variant shown provides approximately the same mean cavity increase Δh as shown in Fig. 13 for a geometric ratio $H/R = 2$. The comparison reveals similar distributions of the strain amplitude. The largest values occur above the edge of the cavity at $z = H$ and $r = R$. It can be also concluded from Fig. 18b that larger H/R ratios do not pose a problem for the stability of the system. Larger H/R ratios reduce the area of the strain amplitude to a smaller proportion of the overburden soil. The greater the overburden height, the lower the strain amplitude at the ground surface.

6. Extrapolation to other geological conditions and further studies

Based on the shown numerical simulations it can be concluded, that a GGES system should not be operated with excessive energy losses. Large energy losses result in large strain amplitudes in the soil, which negatively affect the mechanical behavior of the entire system. An operating limit can be estimated based on the soil mechanical efficiency of $\eta = 95\%$. In fact, this condition limits the mean cavity increase to $\Delta h \approx 0.2$ m and the strain amplitude within the soil to $\varepsilon^{\text{ampl}} \approx 10^{-3}$.

The presented investigations are limited to geometric ratios of $H/R > 2$, and the conclusions drawn are only valid under these conditions. For smaller ratios ($H/R < 2$), the system characteristics become more comparable to the UPHES systems discussed in the introduction. Experimental and numerical studies on such systems have already been conducted [12–16]. While these studies confirm the stability of UPHES systems for small volume amplitudes, failure may occur at larger amplitudes. UPHES systems generally exhibit lower efficiency and capacity while generating significantly larger deformations compared to the proposed GGES system. Additionally, no long-term studies (i.e., over a large number of cycles) are currently available for such UPHES systems.

In contrast, this paper demonstrates the long-term stability of the GGES with geometric ratios $H/R > 2$, operated with a soil mechanical efficiency of $\eta > 95\%$. Under these conditions, only small strain amplitudes occur in the soil and a mechanical failure of the soil can be excluded. The soil strength is then not a limiting factor, since the mechanical loading induced by the energy storage process remains far below the soil's maximum bearing capacity.

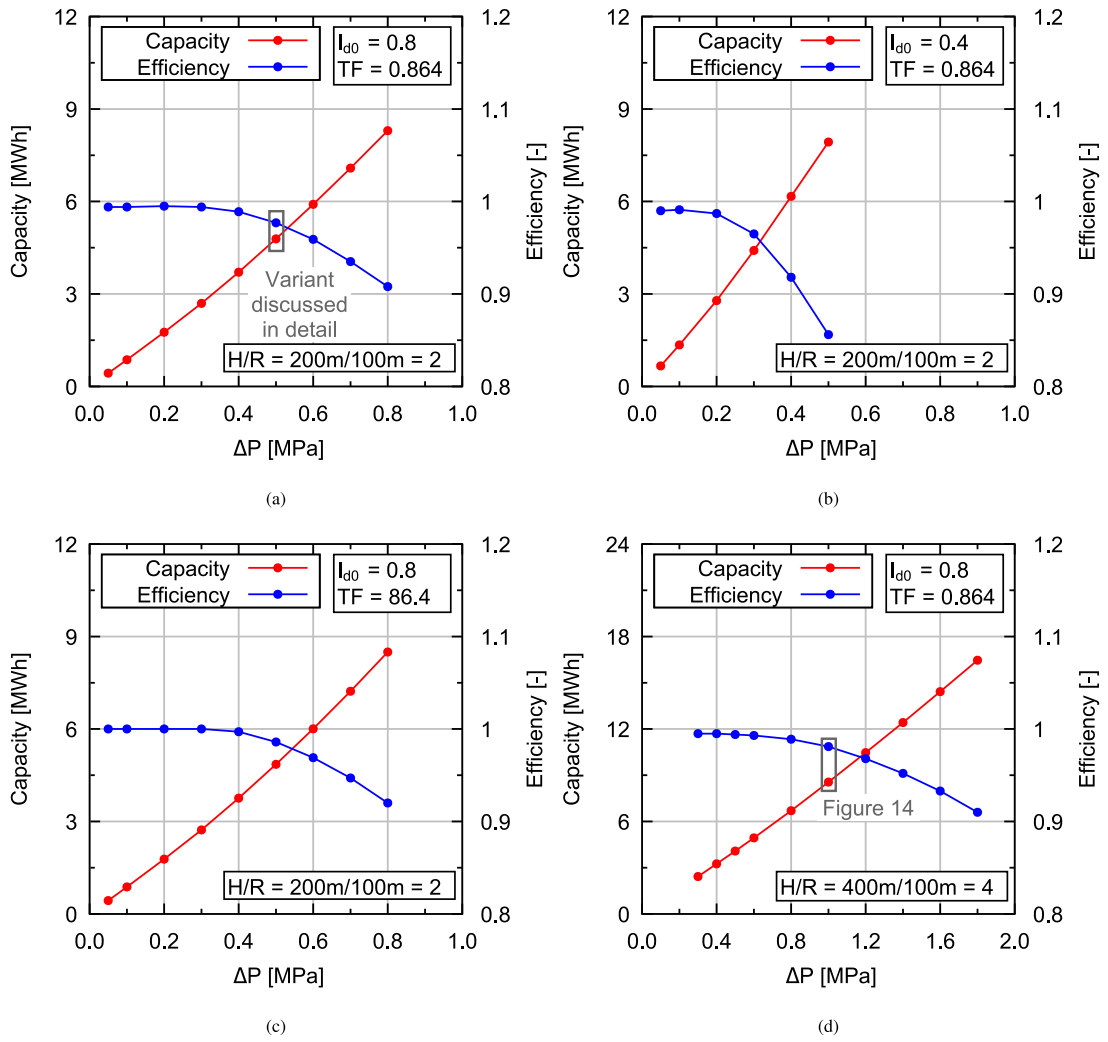

Fig. 16. Capacity and efficiency of the GGES system as a function of the applied pressure difference ΔP for (a) $TF = 0.864$ and $I_{d0} = 0.8$, (b) $TF = 0.864$ and $I_{d0} = 0.4$, (c) $TF = 86.4$ and $I_{d0} = 0.8$, and (d) $TF = 0.864$ and $I_{d0} = 0.8$ but $H = 400$ m $= 4R$.

The numerical analyses were performed using a model sand, Karlsruhe fine sand (KFS). This material is only representative of real in-situ conditions to a limited extent. However, in general, all soil types exhibit similar behavior under high-cyclic loading, although their accumulation rates may vary [25,43]. Interestingly, the restriction to a soil mechanical efficiency of $\eta > 95\%$ implicitly accounts for different geological conditions. The same value of η is reached for different soil types and states (e.g., stiffness, density, homogeneity) at varying pressure amplitudes, as demonstrated by the comparison of simulations for different relative densities (Fig. 16a and b). The normalization using the mean cavity increase Δh (Fig. 17a and b) highlights that the most crucial factor for the overall behavior of a GGES system is the averaged soil weight. While soil stiffness primarily determines the required pressure amplitude and the soil strength is not a crucial factor for a GGES system.

The presented study implicitly assumes that the cavity pressure amplitude remains constant during regular energy storage cycles. In practical applications of a GGES system, irregular charging and discharging cycles are likely to occur. The impact of such non-uniform cyclic loading on the accumulation rate and overall mechanical behavior of a GGES system requires detailed evaluation in future studies. Additionally, the effect of pressure dissipation during the storage period must be investigated. With longer storage duration, a pressure relaxation in the cavity may occur and may lead to additional energy losses. These effects were not considered in the present study and will be addressed in future research. For variants with higher soil mechanical energy losses $\eta < 95\%$, excessive strain amplitudes may develop in the overburden soil and should probably be avoided. Such an operating mode of a GGES is not covered in the present analysis and should be examined in more detail in future studies.

In addition to the isolated GGES system examined in this study, groups of GGES systems might also be analyzed in the future. Such a group arrangement could improve the controllability of energy storage and surface deformations.

7. Conclusion

In the present work, the novel so-called geotechnical gravity energy storage (GGES) system, a large-scale subsurface energy storage technology, is presented. Based on numerical simulations both the energy capacity and efficiency during individual energy storage cycles as well as the long-term stability due to accumulative effects of up to 40 000 energy storage cycles are analyzed. To simulate the mechanical behavior of the overburden soil, an advanced constitutive approach was used by coupling the explicit high-cycle accumulation model (HCA) [22] and the implicit hypoplasticity with intergranular strain model (HP+IS) [23,24]. As a reference variant, a GGES system with an energy storage capacity of up to ≈ 5 MWh and a soil mechanical efficiency of $\eta \approx 98\%$ was investigated. However, the system can be further scaled up [11]. Based on a parametric study, it can be concluded that the GGES system

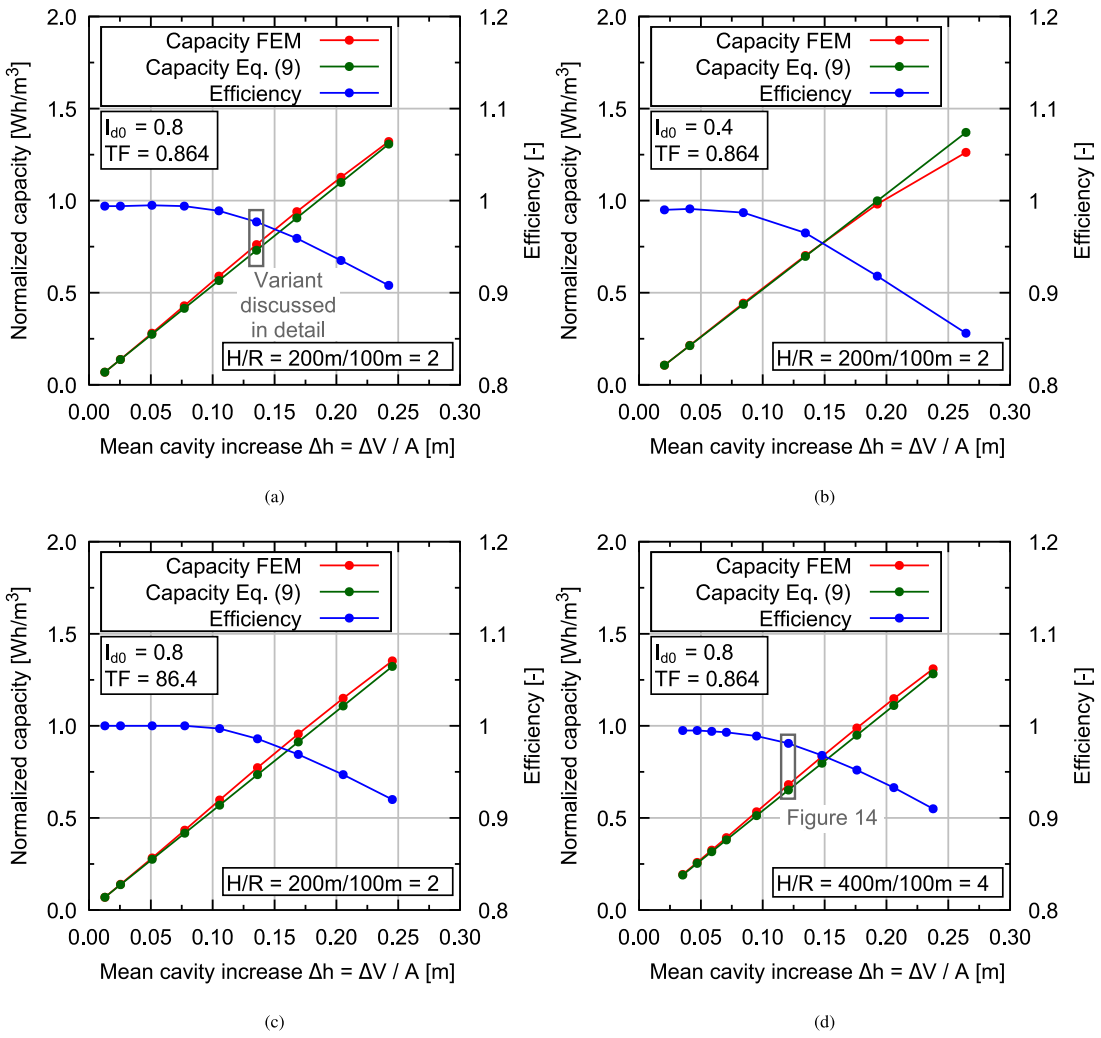

Fig. 17. Normalized capacity and efficiency of the GGES system as a function of the mean cavity increase $\Delta h = \Delta V / A$ (mean cavity increase) per cycle for (a) $TF = 0.864$ and $I_{d0} = 0.8$, (b) $TF = 0.864$ and $I_{d0} = 0.4$, (c) $TF = 86.4$ and $I_{d0} = 0.8$, and (d) $TF = 0.864$ and $I_{d0} = 0.8$ but $H = 400$ m $= 4R$.

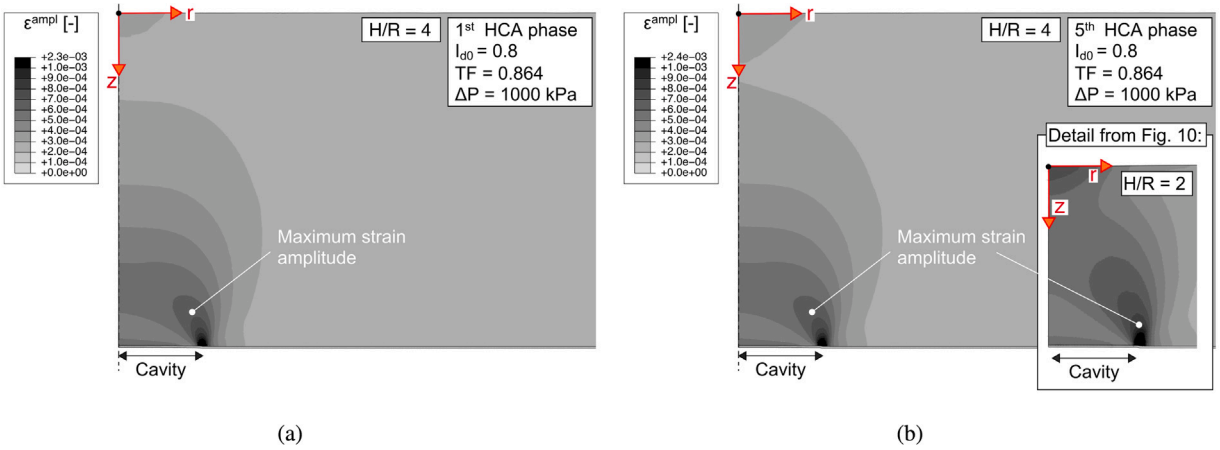

Fig. 18. Spatial distribution of the scalar strain amplitude $\varepsilon^{\text{ampl}}$ in the (a) 1st and the (b) 5th HCA phase for a geometric ratio $H/R = 4$.

- can achieve both large energy capacity and high efficiency.
- is long-term stable for systems with geometric height-to-radius ratios $H/R > 2$, operated with a soil mechanical efficiency of $\eta > 95\%$. Under these conditions, only small strain amplitudes occur in the soil and failure is prevented.
- is only slightly sensitive to soil mechanical constraints such as geological settings, density or permeability.
- exhibits positive aging effects without degradation of the energy capacity and the efficiency over the energy storage cycles.
- leads to positive compaction effects on the overlying soil due to cyclic loading.
- can be designed practically within the above-mentioned limitations using a simple mathematical formula, without the need for complex numerical investigations.

To summarize, it can be concluded that the GGES system is a promising energy storage system for the future, which could become a key element of the green energy transition. The numerical investigations presented in this paper will be complemented by physical tests on the production of the clay-like membrane [19] and model tests on the entire GGES system in the future.

CRediT authorship contribution statement

L. Mugele: Writing – original draft, Visualization, Validation, Methodology, Investigation, Formal analysis, Data curation, Conceptualization. **H.H. Stutz:** Writing – review & editing, Validation, Supervision, Resources, Investigation, Funding acquisition, Conceptualization.

Funding sources

This work was supported by the German Research Foundation (DFG) [Project No. 548951288].

Declaration of competing interest

The authors declare the following financial interests/personal relationships which may be considered as potential competing interests: Hans Henning Stutz has patent #Verfahren und System zur gravitativen Energiespeicherung, Patent Nr. 102022131351 issued to Karlsruher Institut für Technologie. If there are other authors, they declare that they have no known competing financial interests or personal relationships that could have appeared to influence the work reported in this paper.

Acknowledgments

The authors would like to thank Prof. G. Gudehus for purposeful discussions, Prof. A. Niemunis for helpful comments on the numerical aspects and the corresponding implementations and C. Directör for detailed proofreading. The authors are grateful to DFG, Germany for the financial support.

Data availability

Data will be made available on request.

References

[1] O. Schmidt, I. Staffell, Monetizing Energy Storage: A Toolkit to Assess Future Cost and Value, Oxford University Press, 2023.
[2] Fraunhofer-Institut für Solare Energiesysteme ISE, Jährlicher Anteil Erneuerbarer Energien an der öffentlichen nettostromerzeugung und Last in der europäischen Union, 2024, https://www.energy-charts.info.
[3] IEA - International Energy Agency, Renewable energy market update - June 2023: Outlook for 2023 and 2024, 2023.
[4] D. Gielen, F. Boshell, D. Saygin, M.D. Bazilian, N. Wagner, R. Gorini, The role of renewable energy in the global energy transformation, Energy Strat. Rev. 24 (2019) 38–50, http://dx.doi.org/10.1016/j.esr.2019.01.006.
[5] N.L. Panwar, S.C. Kaushik, S. Kothari, Role of renewable energy sources in environmental protection: A review, Renew. Sustain. Energy Rev. 15 (3) (2011) 1513–1524, http://dx.doi.org/10.1016/j.rser.2010.11.037.
[6] H.-W. Sinn, Buffering volatility: A study on the limits of Germany's energy revolution, Eur. Econ. Rev. 99 (2017) 130–150, http://dx.doi.org/10.1016/j.euroecorev.2017.05.007.
[7] M. Aneke, M. Wang, Energy storage technologies and real life applications – A state of the art review, Appl. Energy 179 (2016) 350–377, http://dx.doi.org/10.1016/j.apenergy.2016.06.097.
[8] T.M. Gür, Review of electrical energy storage technologies, materials and systems: challenges and prospects for large-scale grid storage, Energy Environ. Sci. 11 (10) (2018) 2696–2767, http://dx.doi.org/10.1039/C8EE01419A.
[9] A. Blakers, M. Stocks, B. Lu, C. Cheng, A review of pumped hydro energy storage, Prog. Energy 3 (2) (2021) 022003, http://dx.doi.org/10.1088/2516-1083/abeb5b.
[10] F. Geth, T. Brijs, J. Kathan, J. Driesen, R. Belmans, An overview of large-scale stationary electricity storage plants in Europe: Current status and new developments, Renew. Sustain. Energy Rev. 52 (2015) 1212–1227, http://dx.doi.org/10.1016/j.rser.2015.07.145.
[11] G. Gudehus, C. Lempp, F. Schilling, H.H. Stutz, Earth batteries, Acta Geotech. (under preparation).
[12] J. Olsen, K. Paasch, B. Lassen, C.T. Veje, A new principle for underground pumped hydroelectric storage, J. Energy Storage 2 (2015) 54–63, http://dx.doi.org/10.1016/j.est.2015.06.003.
[13] K.K. Sørensen, H.H. Stutz, B.-R. Phivos, L. Martin, Conceptual physical modelling of a subsurface geomembrane energy storage system, in: Proceedings of the 20th International Conference on Soil Mechanics and Geotechnical Engineering, Sydney, 2021.
[14] A. Franza, K.K. Sorensen, H.H. Stutz, A. Pettey, C. Heron, A.M. Marshall, Field and centrifuge modelling of a pumped underground hydroelectric energy storage system in sand, in: 10th International Conference on Physical Modelling in Geotechnics, Daejeon, 2022.
[15] P. Norlyk, K. Sørensen, L.V. Andersen, K.K. Sørensen, H.H. Stutz, Holistic simulation of a subsurface inflatable geotechnical energy storage system using fluid cavity elements, Comput. Geotech. 127 (2020) 103722, http://dx.doi.org/10.1016/j.compgeo.2020.103722.
[16] H.H. Stutz, P. Norlyk, K. Sørensen, L.V. Andersen, K.K. Sørensen, J. Clausen, Finite element modelling of an energy-geomembrane underground pumped hydroelectric energy storage system, E3S Web Conf. 205 (2020) 07001, http://dx.doi.org/10.1051/e3sconf/202020507001.
[17] K.K. Sørensen, H.C. Feijborg, T. Labda, H. Wetzel, P. Materna, A. Svendstrup-Bjerre, B. Nielsen, J. Vedde, H.J. Brodersen, Underground pumped hydro storage (UPHS) - Final report, 2022.
[18] G. Gudehus, C. Lempp, F. Schilling, H.H. Stutz, Verfahren und system zur gravitativen Energiespeicherung, 2024, German patent number 102022131351.
[19] J.C. Walter, L. Mugele, G. Gudehus, H.H. Stutz, Underground energy storage by means of injected bentonite double membranes, in: 3rd International Conference on Energy Geotechnics, Paris, 2025.
[20] B. Zakeri, S. Syri, Electrical energy storage systems: A comparative life cycle cost analysis, Renew. Sustain. Energy Rev. 42 (2015) 569–596, http://dx.doi.org/10.1016/j.rser.2014.10.011.
[21] A.A. Kebede, T. Kalogiannis, J. Van Mierlo, M. Berecibar, A comprehensive review of stationary energy storage devices for large scale renewable energy sources grid integration, Renew. Sustain. Energy Rev. 159 (2022) 112213, http://dx.doi.org/10.1016/j.rser.2022.112213.
[22] A. Niemunis, T. Wichtmann, T. Triantafyllidis, A high-cycle accumulation model for sand, Comput. Geotech. 32 (4) (2005) 245–263, http://dx.doi.org/10.1016/j.compgeo.2005.03.002.
[23] A. Niemunis, I. Herle, Hypoplastic model for cohesionless soils with elastic strain range, Mech. Cohesive- Frict. Mater. 2 (4) (1997) 279–299, http://dx.doi.org/10.1002/(SICI)1099-1484(199710)2:4<279::AID-CFM29>3.0.CO;2-8.
[24] P.-A. von Wolffersdorff, A hypoplastic relation for granular materials with a predefined limit state surface, Mech. Cohesive- Frict. Mater. 1 (3) (1996) 251–271, http://dx.doi.org/10.1002/(SICI)1099-1484(199607)1:3<251::AID-CFM13>3.0.CO;2-3.
[25] T. Wichtmann, Soil Behaviour Under Cyclic Loading - Experimental Observations, Constitutive Description and Applications (Habilitation thesis), Institute of Soil Mechanics and Rock Mechanics (IBF), Karlsruhe Institute of Technology (KIT), issue 181, Karlsruhe, 2016.
[26] L. Mugele, A. Niemunis, L. A., H.H. Stutz, Investigations on a novel gravitational energy storage system using a high-cycle accumulation model, in: Proceedings 10th NUMGE 2023, London, 2023.
[27] V.A. Osinov, Some aspects of the boundary value problems for the cyclic deformation of soil, in: T. Triantafyllidis (Ed.), Holistic Simulation of Geotechnical Installation Processes. Theoretical Results and Applications, vol. 82, Springer, Cham, 2017, pp. 150–167, http://dx.doi.org/10.1007/978-3-319-52590-7_6.
[28] I. Herle, G. Gudehus, Determination of parameters of a hypoplastic constitutive model from properties of grain assemblies, Mech. Cohesive- Frict. Mater. 4 (5) (1999) 461–486, http://dx.doi.org/10.1002/(SICI)1099-1484(199909)4:5<461::AID-CFM71>3.0.CO;2-P.
[29] D. Mašín, Modelling of Soil Behaviour with Hypoplasticity, Springer International Publishing, Cham, 2019, http://dx.doi.org/10.1007/978-3-030-03976-9.
[30] L. Knittel, A. Lamparter, A. Niemunis, H.H. Stutz, The high-cyclic model for sand tested beyond the usual ranges of application, Acta Geotech. (2023) 1–12, http://dx.doi.org/10.1007/s11440-023-02031-y.
[31] T. Wichtmann, T. Triantafyllidis, An experimental database for the development, calibration and verification of constitutive models for sand with focus to cyclic loading: part II—tests with strain cycles and combined loading, Acta Geotech. 11 (4) (2016) 763–774, http://dx.doi.org/10.1007/s11440-015-0412-x.
[32] T. Wichtmann, T. Triantafyllidis, An experimental database for the development, calibration and verification of constitutive models for sand with focus to cyclic loading: part I—tests with monotonic loading and stress cycles, Acta Geotech. 11 (4) (2016) 739–761, http://dx.doi.org/10.1007/s11440-015-0402-z.

[33] P. Staubach, T. Wichtmann, Long-term deformations of monopile foundations for offshore wind turbines studied with a high-cycle accumulation model, Comput. Geotech. 124 (2020) 103553, http://dx.doi.org/10.1016/j.compgeo.2020.103553.
[34] J. Zürn, L. Mugele, H.H. Stutz, Novel experimental method for rate-independent triaxial tests under partial drainage condition, Géotech. Lett. 14 (3) (2024) 100–105, http://dx.doi.org/10.1680/jgele.23.00120.
[35] A. Niemunis, IncrementalDriver: programmer's manual, 2022.
[36] D. Wegener, I. Herle, Zur Steifigkeit bei kleinen Dehnungen im Rahmen der Hypoplastizität, Geotechnik 35 (4) (2012) 229–235, http://dx.doi.org/10.1002/gete.201200006.
[37] L. Mugele, A. Niemunis, H.H. Stutz, Neohypoplasticity Revisited, Int. J. Numer. Anal. Methods Geomech. 48 (1) (2024) 311–331, http://dx.doi.org/10.1002/nag.3640.
[38] L. Mugele, H.H. Stutz, D. Mašín, Generalized intergranular strain concept and its application to hypoplastic models, Comput. Geotech. (173) (2024) 106480, http://dx.doi.org/10.1016/j.compgeo.2024.106480.
[39] A.L. Petalas, Y.F. Dafalias, A.G. Papadimitriou, SANISAND-F: Sand constitutive model with evolving fabric anisotropy, Int. J. Solids Struct. 188–189 (2020) 12–31, http://dx.doi.org/10.1016/j.ijsolstr.2019.09.005.
[40] E. Bauer, Calibration of a comprehensive hypoplastic model for granular materials, Soils Found. 36 (1) (1996) 13–26, http://dx.doi.org/10.3208/sandf.36.13.
[41] A. Niemunis, I. Melikayeva, Improved integration of High-Cycle accumulated strain using hierarchical and EAS finite elements, in: T. Triantafyllidis (Ed.), Holistic Simulation of Geotechnical Installation Processes, Springer, Cham, 2015, pp. 181–205, http://dx.doi.org/10.1007/978-3-319-18170-7_10.
[42] J.B. Burland, C.P. Wroth, Settlement of buildings and associated damage, in: British Geotechnical Society Conference on Settlement of Structures, Cambridge, 1975.
[43] P. Staubach, J. Machaček, M. Tafili, T. Wichtmann, A high-cycle accumulation model for clay and its application to monopile foundations, Acta Geotech. 17 (3) (2022) 677–698, http://dx.doi.org/10.1007/s11440-021-01446-9.